

www.acsanm.org Article

Tunable Three-Phase Co-CeO₂-BaTiO₃ Hybrid Metamaterials with Nano-Mushroom-Like Structure for Tailorable Multifunctionalities

Bethany X. Rutherford, Bruce Zhang, Matias Kalaswad, Zihao He, Di Zhang, Xuejing Wang, Juncheng Liu, and Haiyan Wang*



Cite This: ACS Appl. Nano Mater. 2022, 5, 6297-6304



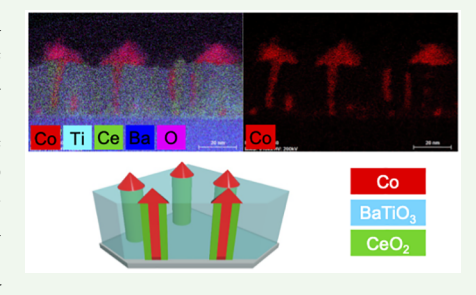
ACCESS

Metrics & More

Article Recommendations

s Supporting Information

ABSTRACT: Recent studies in complex nanocomposite thin films have brought forth interesting morphologies and physical properties and thus great potential for future devices. This study presents the formation of a nanomushroom structure developed from a complex three-phase nanocomposite system, i.e., the Co–CeO₂–BaTiO₃ (Co–CeO₂–BTO) system. Via varying the oxygen partial pressure during deposition, the Co–CeO₂–BTO system growth shows a microstructure tuning of vertically aligned Co nanopillars in a CeO₂–BTO composite matrix processed in vacuum to the Co nanomushroom-like structures under 200 mTorr oxygen. Such morphology tuning results in interesting physical property tuning such as magnetic anisotropy, optical anisotropy, and dielectric function tuning. This study suggests the effectiveness of morphology



tuning via complex three-phase nanocomposite designs and processing condition variation. The resultant three-phase nanocomposite structures present great potential to address the needs on multifunctional hybrid materials for nanoscale optical and magnetic device demonstrations.

KEYWORDS: three-phase nanocomposite, thin film, morphology, ferromagnetic, hyperbolic, surface plasmon resonance (SPR)

■ INTRODUCTION

Novel hybrid metamaterials that combine two or more materials for artificially tuned physical properties and multifunctionalities have attracted great interest because of their enormous versatility in materials selection and great potential in electronics and optical devices. 1,2 In these applications, the structure and growth of hybrid metamaterials play a crucial role in the properties of the materials, necessitating controlled processing techniques and methods. There are primarily two classes of approaches for processing hybrid metamaterials: topdown approaches such as lithography and patterning^{3,4} and bottom-up thin-film growth methods via multilayer stacking⁵ or self-assembled growth.^{6,8} Evolving as one of the selfassembled hybrid thin films, vertically aligned nanocomposites (VAN) effectively combine two epitaxial phases in a vertical co-grown columnar fashion on various substrates.^{7,9,10} A variety of nanostructures have been demonstrated: nanopillar-in-matrix,⁵ nanochecker-board structure,¹¹ and nanomaze-like domains. 12 The VAN structure has demonstrated a variety of functionalities including plasmonic and optical property tuning, 2,13 ferroelectric-magnetic coupling for multiferroics, 14-16 magneto-optical coupling, 16-18 and superior ionic transport properties. 19-21

VANs present advantages over other hybrid metamaterial designs in their nanoscale features, epitaxial film quality, and highly anisotropic physical properties. 4-6,16 Most of the previous VAN studies have examined oxide—oxide two-phase systems, where one phase has strong physical properties and

the second oxide phase has strong vertical strain coupling across the interfaces. \$4,6,16,22\$ Recently, oxide-metal VAN systems have evolved as a new class of VAN combining two very dissimilar phases—i.e., oxides and metals for exotic optical properties—such as tunable hyperbolic optical responses, epsilon near-zero (ENZ) wavelength, and enhanced nonlinearities via second harmonic generation measurements. \$16-18\$ This new class of VANs with their unique properties and tunability, introduces new opportunities in plasmonics and optic designs for all-optical integrated circuits.

Tuning the physical properties in VAN thin films can be achieved by film morphology modulation via adjusting deposition parameters (e.g., deposition rate, deposition temperature, substrate treatments, etc.). ^{1,3,5} For example, prior work has demonstrated that the deposition frequency can effectively vary the nanopillar dimension from 7 to 13.5 nm in the BiFeO₃–Sm₂O₃ system and thus impact the overall physical properties. ⁸ Oxygen partial pressure effectively tunes the growth kinetics and thus the resultant film morphology from hexagonal nanopillars to irregularly shaped and oriented nanopillars in ZnO–Au VAN films. ² Substrate strain also plays

Received: January 25, 2022 Accepted: April 11, 2022 Published: April 25, 2022





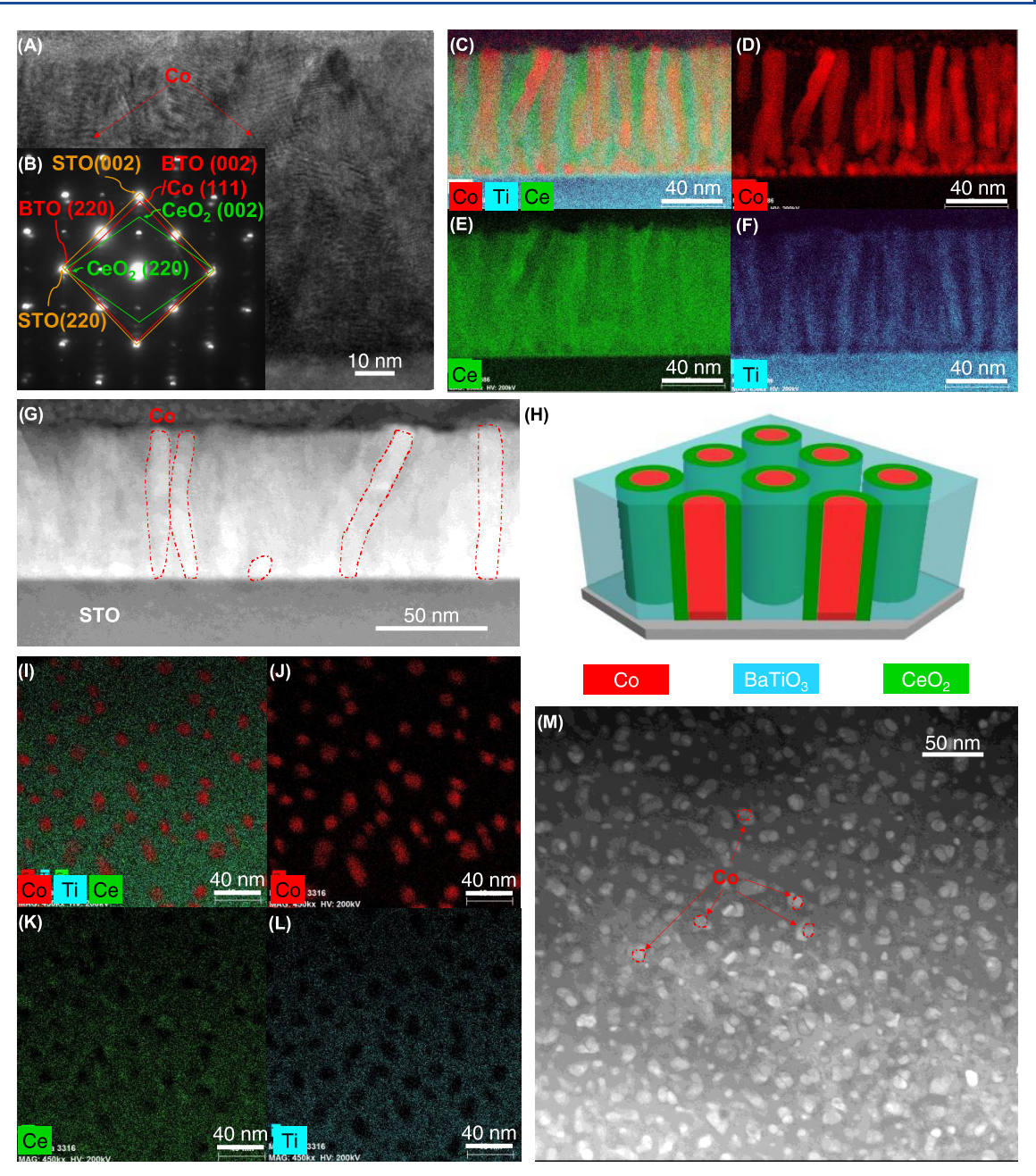


Figure 1. (A) Cross-sectional TEM image of Co–CeO₂–BTO grown in vacuum, (B) diffraction pattern of the film and STO substrate, (C) cross-sectional composite EDX mapping of Co–Ce–Ti, (D) cross-sectional EDX mapping of Co, (E) cross-sectional EDX mapping of Ce, (F) cross-sectional EDX mapping of Ti, (G) cross-sectional STEM image of Co–CeO₂–BTO grown in vacuum, (H) schematic drawing of Co–CeO₂–BTO grown in vacuum, (I) plan-view composite EDX mapping of Co–Ce–Ti, (J) plan-view EDX mapping of Co, (K) plan-view EDX mapping of Ce, (L) plan-view EDX mapping of Ti, and (M) plan-view STEM image of Co–CeO₂–BTO grown in vacuum.

a critical role in the overall two-phase distribution, and a unique strain compensation model has predicted the potential ordering of the two phases by selecting two phases with opposite strain states with the substrate. Most VAN tuning has been demonstrated in two-phase VAN designs with very limited demonstrations in three-phase systems. 1,16,18

In this work, we demonstrate a new approach for effective VAN morphology tuning by incorporating novel three-phase nanocomposite designs. We have selected a complex metal-oxide—oxide- three-phase system, $\text{Co-CeO}_2\text{-BaTiO}_3$ (Co-CeO₂–BTO) for demonstration. Co was selected because of its strong ferromagnetic properties in combination with its unique plasmonic properties and the surface plasmon

resonance (SPR) effect. Previous studies have also shown that Co and Co–alloy nanocomposite materials in oxide matrixes have very interesting size-dependent magnetic and optical properties. Co metal has successfully grown in oxide matrices to create nanocomposite materials in BaZrO₃–Co, BTO–Co, CeO₂–Co, and Zr₂O–Co systems. Co–CeO₂ nanocomposite thin films specifically have produced thin-film materials with Co features as small as 3 nm. Additionally, it can be considered as a cheaper alternative compared to the most common plasmonic materials in SPR sensors: Au or Ag. Via oxygen partial pressure control, the overall morphology of the three-phase system can be easily tuned as illustrated in Figure 1. In this work, oxygen

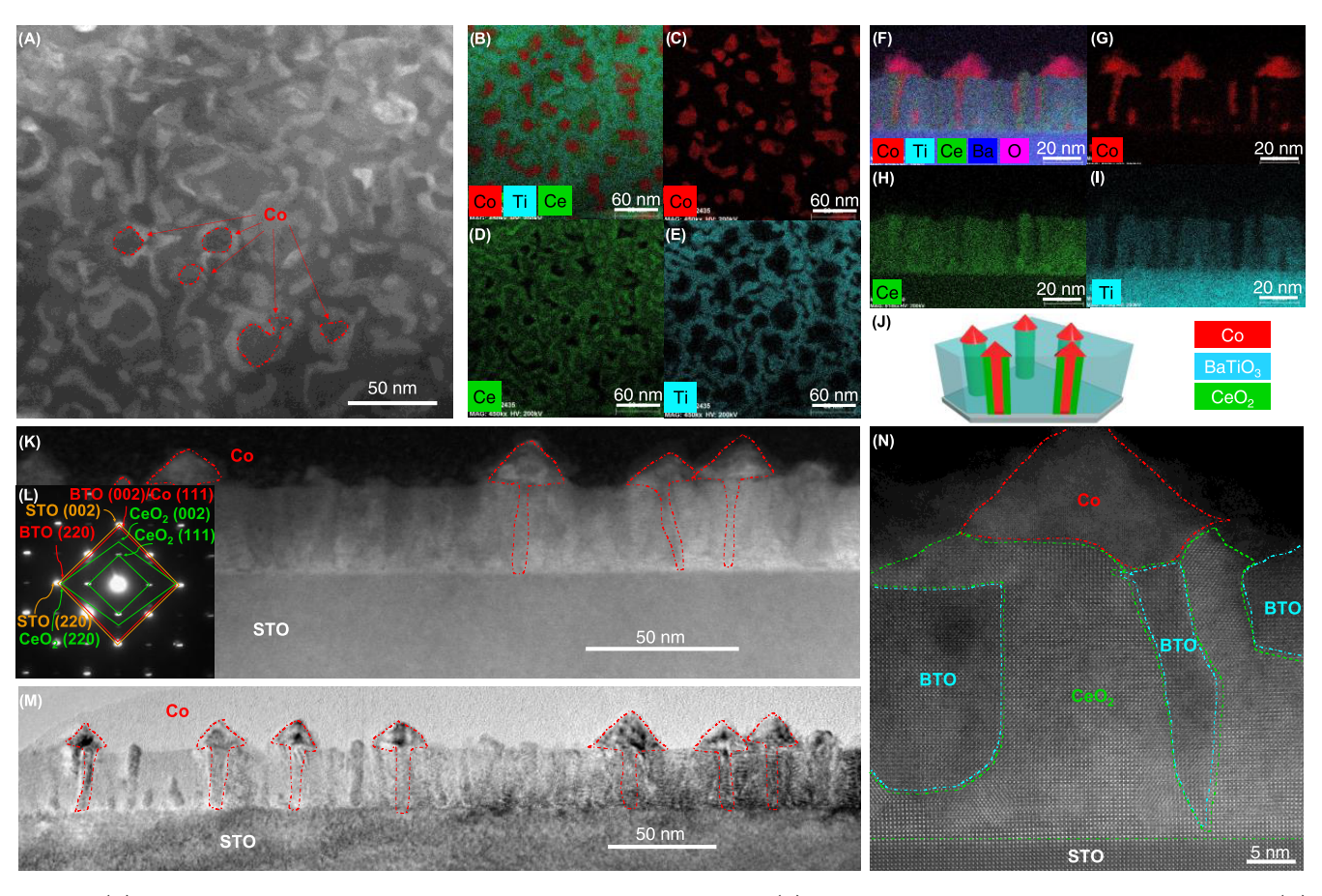


Figure 2. (A) Plan-view STEM image of Co–CeO₂–BTO grown in 200 mTorr O₂, (B) composite plan-view EDX mapping of Co–Ce–Ti, (C) plan-view EDX mapping of Co, (D) plan-view EDX mapping of Ce, (E) plan-view EDX mapping of Ti, (F) cross-sectional composite EDX mapping of Co–Ce–Ti, (G) cross-sectional EDX mapping of Co, (H) cross-sectional EDX mapping of Ce, (I) cross-sectional EDX mapping of Ti, (J) schematic drawing of Co–CeO₂–BTO grown in 200 mTorr O₂, (K) cross-sectional STEM image of Co–CeO₂–BTO grown in 200 mTorr O₂, (L) diffraction pattern of the film, (M) cross-sectional TEM image of Co–CeO₂–BTO grown in 200 mTorr O₂, and (N) high-resolution cross-sectional TEM image of a nanomushroom.

partial pressure varied from low to high pressure during growth. A higher amount of oxygen during oxide thin-film growth promotes their nucleation and growth on the substrate surface over a metallic phase. Reducing the oxygen present reduces the growth kinetics for oxide materials, allowing a metal phase to nucleate at a faster rate than when grown in an oxygen-filled environment. The differing nucleation and growth rates will affect the morphology, tuning the different physical properties. Detailed property explorations, including magnetic and optical property measurements, were conducted to correlate the tunable morphologies with their resultant physical properties. This study presents a new approach in achieving the morphology control of the nanopillars that have great potential as plasmonic sensors and nanoantennas in nanophotonic devices.

EXPERIMENTAL SECTION

Pulsed laser deposition (PLD) with a KrF laser (Lambda Physik, $\lambda=248\,$ nm) at 5 Hz was used to fabricate nanocomposite thin-film samples. The laser energy was set at 420 mJ. The nanocomposite thin films were made with a composite target of BTO/CeO₂/Co with a molar ratio of 1:1:2 and grown on single-crystal SrTiO₃ (STO) (001) substrates in either 200 mTorr oxygen or vacuum at 750 °C. After deposition, the thin films were cooled at 5 °C/min.

X-ray diffraction (XRD) (PANalytical Empyrean diffractometer) was used to determine potential peak shifting due to oxygen

background pressure tuning. Transmission electron microscopy (TEM) (FEI TALOS F200X) was used to determine the nanostructure of the films with energy-dispersive X-ray spectroscopy (EDX) mapping and high-resolution scanning transmission electron microscopy (STEM). TEM samples were created using the standard manual preparation process: grinding, dimpling, and ion milling (PIPS II Gatan).

A magnetic property measurement system (MPMS) (MPMS Model 3, Quantum Design) measured the magnetic properties for inplane and out-of-plane directions of each film. Optical property measurements were conducted using a RC2 spectroscopic ellipsometer (J.A. Woollam Company), where the angles measured were 30, 45, and 60° with a spectrum range of 210–2500 nm. The psi and delta data were fit with a B-spline model to determine anisotropic permittivity. COMSOL Multiphysics Wave Optics Module was applied for the optical simulation. Optical constants for Co, CeO₂, and BTO were directly taken from the software database. The simulated geometry was retrieved based on the plan-view and crosssectional TEM images, including average pillar diameter (\overline{d}) , average interpillar distance (\overline{l}) , and film thickness (t), which are $\overline{d} = 4.5$ nm, \overline{l} = 38 nm, and t = 27 nm for the nanomushroom structure and $\overline{d} = 5$ nm, $\overline{l} = 25$ nm, and t = 60 nm for the nanopillar structure. The dimension of the nanomushroom "head" is estimated to be 10 nm in height and 18 nm in width, respectively. A normal incidence depolarized electromagnetic field was applied with two ports on the top and bottom of the model.

RESULTS AND DISCUSSION

Interestingly, via the oxygen partial pressure control, the morphology of the Co-CeO₂-BTO system was effectively tuned, as shown in Figures 1 and 2 for the vacuum and 200 mTorr grown samples, respectively. For the vacuum-grown sample, it is obvious that Co forms uniform and straight vertical nanopillars (~11.1 nm in average diameter) with a unique core-shell structure or partial core-shell structure produced by the CeO₂ phase preferentially surrounding the Co nanopillars. Surrounding the CeO2 phase shell is the BTO phase, which has a tetragonal perovskite structure with a larger lattice parameter of 3.99 Å. The STO substrate has a lattice parameter of 3.91 Å, which is the closest to BTO. Thus, it is consistent with other three-phase works where the closest matching phase to the substrate has the tendency to be the matrix phase. It is noted that the Co nanopillars are very thin (10 nm or less), and the domains from CeO₂ and BTO are also very small. It posed challenges in nanostructural characterizations of all three phases. However, based on EDX mappings in plan-view and cross section, it is evident that the Co phase has grown into uniform nanopillars uniformly distributed in the CeO₂ and BTO matrix.

When the three-phase system was grown under the same growth conditions with the exception of the 200 mTorr oxygen environment, the overall VAN structure is still present; however, the Co nanopillars assemble into an interesting nano-mushroom-like morphology combining the "mushroom stem" regions (i.e., the Co nanopillars with the reduced average diameter of 4.3 nm) and the "mushroom cap" regions (i.e., the Co clusters on top of the nanopillars). This unique nanomushroom-like morphology could be attributed to the altered growth kinetics under 200 mTorr. Under 200 mTorr, the plume is more confined, and the growth rate of oxides increases. In addition, the morphology distribution of oxides and metal phases changes during the initial growth. This effect is evident in the cross-sectional TEM images in Figures 1A-G and 2F-M. This results in much smaller nucleation sites for Co and thus much smaller Co nanopillars. However, this also leads to the accumulation of the excess Co during growth and thus the formation of the "mushroom cap." In comparison, the density of the Co nanopillar distribution throughout the oxide matrix under 200 mTorr is much smaller than that of the films grown under vacuum (Figure 2K,M). Figure 2N shows distinct lattices from the Co mushroom regions and the stem regions, with much smaller lattice spacings compared to the oxide matrix lattice. It is possible that some parts of the mushroom cap experienced oxidation during the annealing process postdeposition. The majority of the nanomushroom is still believed to be Co evidenced by the lattice structure (Figure 2N). To confirm that, Figure S1 shows a high-resolution STEM image of the Co nanomushroom cap relative to the BTO oxide matrix with the *d*-spacing measured and labeled for both regions. The corresponding fast Fourier transform (FFT) analysis for both the Co and the BTO regions was conducted and shown in Figure S1. The d-spacing of Co was measured to be ~ 0.189 nm for Co (002) and ~ 0.391 nm for BTO (001). The Co d-spacing measured is consistent with the cubic Co lattice. The Co and BTO regions show clearly different diffraction patterns based on the FFT analysis results. The influence of growth kinetics on the out-of-plane strain in the films is also supported by the XRD results, where BTO peaks are shifted to higher angles, indicating that the BTO out-ofplane lattice is under compression when grown under vacuum conditions (Figure 3). Both oxide phases become more

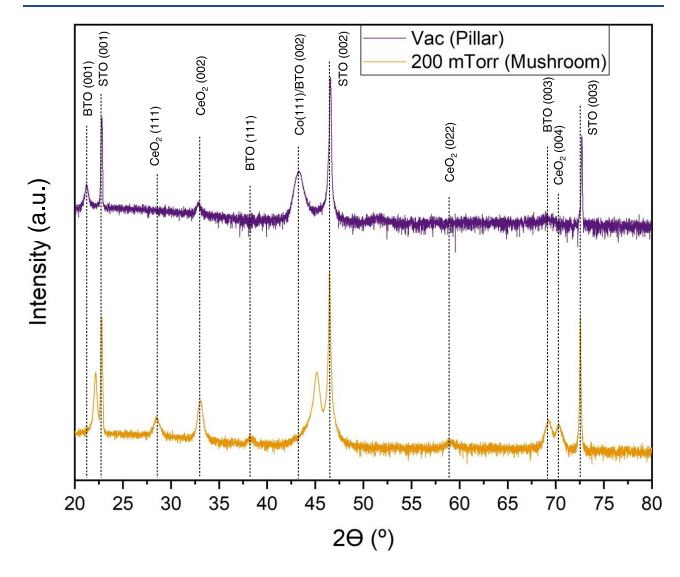


Figure 3. XRD data of Co–CeO₂–BTO thin films deposited under vacuum and 200 mTorr.

dominant when grown in oxygen as all of the oxide peak intensities are higher than that of a vacuum-grown film. The peaks in Figure 3 are also reflected in the TEM diffraction patterns in Figures 1B and 2L. The nanomushroom structure diffraction patterns have an additional orientation of CeO_2 (111).

In addition to the growth kinetics of the oxides versus the Co metal, the interfacial relationships between the phases are also important. Based on the EDX data (Figures 1C-F,I-L, and 2B-I), the interface between the Co and oxide phases is sharp and distinct, whereas the interface between CeO2 and BTO is less clear. It is interesting to note that the CeO₂ phase tends to grow adjacent to the Co metal as evidenced by the higher intensity of Ce around the Co pillars. The less clear interface between the CeO2 and BTO phases could be due to less obvious phase separation between the oxides. The interfaces between the CeO2 and BTO phases for the film grown under 200 mTorr (nanomushroom case, Figure 2) are much cleaner and sharper than that in the film under vacuum (nanopillar case, Figure 1). This might be due to the growth kinetic differences and the oxygen content difference under different oxygen back pressure. Under 200 mTorr, the plume of all species is well confined and the density of adatoms is higher than that of the vacuum case and thus result in more effective nucleation and growth of oxides and better oxide phase separation. However, the metal growth could be limited under 200 mTorr and thus forms much thinner pillars in the initial growth (i.e., the nanomushroom stem). In addition to the interfaces between the film phases, the interface between the substrate and the film is important as the similar lattice parameter and surface energy between the STO and oxide phases promotes the nucleation and growth of oxides, the fact that the initial composite target composition is 1:1 molar ratio of metal:oxides.

In terms of magnetic properties of these hybrid nanocomposites, the nanopillar sample grown under vacuum (in purple) maintains higher magnetization and coercivity than those of the mushroom counterpart (in orange), as seen in

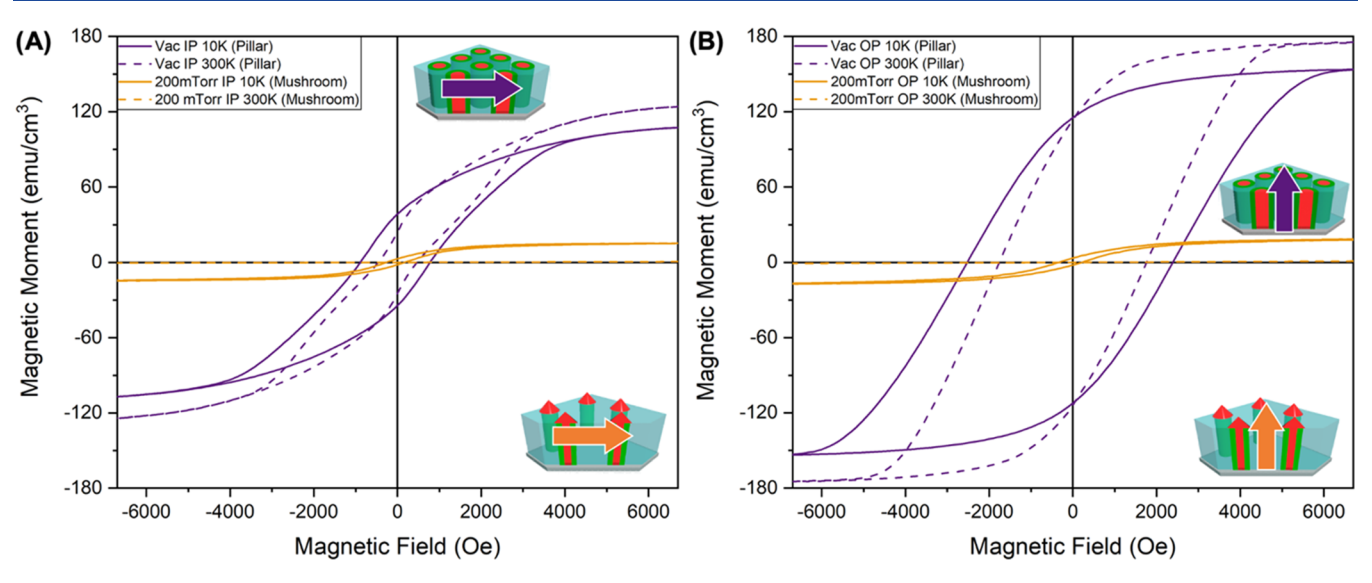


Figure 4. (A) Magnetization data for the in-plane direction for vacuum-grown nanopillars (purple) and 200 mTorr O₂-grown nanomushrooms (orange) and (B) Magnetization data for the out-of-plane direction for vacuum-grown nanopillars (purple) and 200 mTorr O₂-grown nanomushrooms (orange).

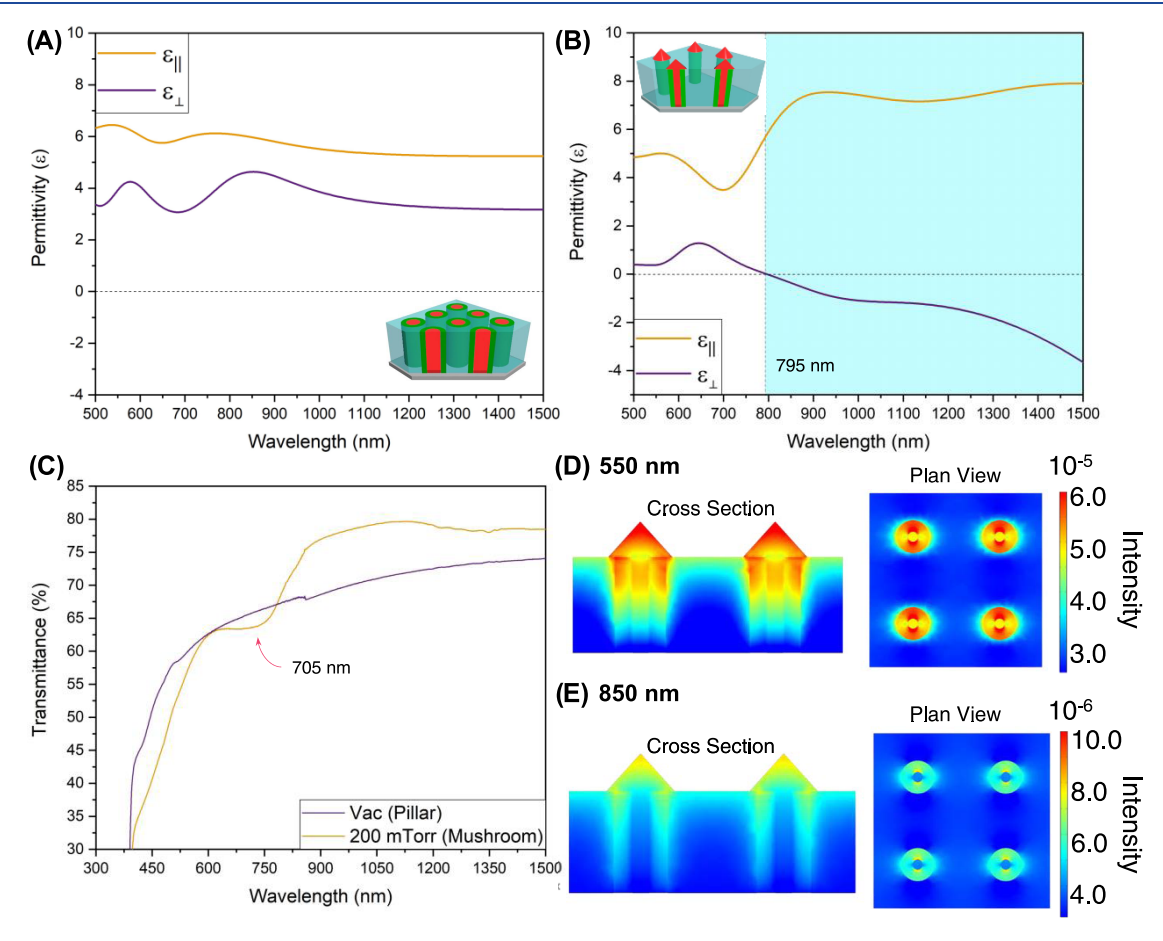


Figure 5. (A) Optical permittivity of nanopillar structure, (B) Optical permittivity and hyperbolic behavior of nanomushroom structure, (C) transmittance of nanopillar (purple) and nanomushroom (orange) films, and (D) COMSOL simulation of nanomushroom at 550 nm for cross section and plan-view, and (E) COMSOL simulation of nanomushroom at 850 nm for cross section and plan-view.

Figure 4. The VAN structure has an in-plane magnetic saturation of 125 and 105 emu cm⁻³ at 300 and 10 K and an out-of-plane magnetic saturation of 175 and 155 emu cm⁻³ at 300 and 10 K, respectively. The VAN structure also has an in-plane coercivity of 500 and 800 Oe at 10 and 300 K and an

out-of-plane coercivity of 1800 and 2400 Oe at 10 and 300 K, respectively. The results suggest an obvious out-of-plane magnetic anisotropy in the VAN sample. The mushroom structure presents a much weaker magnetic response, i.e., an in-plane magnetic saturation of 15 emu cm⁻³ and an out-of-

plane magnetic saturation of 18 emu cm⁻³ at 10 K. One possible reason for the weaker magnetic response is that at 300 K the mushroom structure could show superparamagnetic properties rather than ferromagnetic due to the very small size of the mushroom stem being 4.3 nm in diameter. Previous reports have shown that magnetic Co structures and high percentage Co-alloy structures present a superparamagnetic limit when their particle size reduces to 5-8 nm. 24,25,27,33,34 Co has also been shown to vary the superparamagnetic domain size with temperature. 24,35 The small size and very low density of the Co mushroom nanostructure both contribute to their overall magnetic behavior and explain the weak ferromagnetic behavior at 10 K and paramagnetic behavior at room temperature. More specifically, the very thin nanopillars (~4.3 nm) and low pillar density in the nanomushroom film result in a lower amount of Co in the film compared to the wide nanopillars and high pillar density in the VAN sample. Thus, much weaker ferromagnetic responses were observed in the nanomushroom sample compared to the nanopillar one.

In terms of optical response, the nanomushroom structure presents interesting characteristics. As seen in Figure 5A, the VAN structure acts overall as a dielectric material. The nanomushroom structure acts as a metamaterial that behaves hyperbolically in iso-frequency space at 795 nm, i.e., the out-ofplane permittivity becomes negative while the in-plane permittivity remains positive and increases in value (Figure 5B). The largest difference in the optical permittivity is the perpendicular component of the nanomushroom film becoming negative. This change can be attributed to the distribution of Co in the nanomushroom structure being more on top of the film than in the nanopillar structure. Specifically, vertical and thin metallic Co nanopillars present a negative permittivity value out-of-plane, while the dielectric oxides in the matrix contribute to the positive permittivity values in-plane. In terms of transmittance (Figure 5C), the mushroom structure shows SPR within the wavelength range between 500 and 800 nm with a dip at 705 nm, whereas the VAN nanopillar structure does not show obvious resonance, which indicates that the nanopillar structure shows a weaker SPR effect than the nanomushroom hybrid film. Based on the transmittance spectra of both films, the optical simulation was conducted using COMSOL Multiphysics software (see the Experimental Section and Figure S2 for more details). Figure 5D,E exhibits electric field maps (EFMs) for the nanomushroom Co-CeO₂-BTO hybrid film at 550 and 850 nm, respectively. As shown in Figure 5D, it can be clearly seen that the "mushroom head" structure enhanced the SPR effect remarkably with the highest intensity on the top. As the light penetrates the film, the SPR effect intensity degrades rapidly. Because the overall film thickness is merely around 30 nm, most of the film is showing noticeable plasmon resonance under the 550 nm light illumination. On the other hand, Figure 5E shows a less obvious SPR effect within the nanomushroom film. By comparing the intensity scale bar shown on the right, it is clearly seen that the SPR intensity at 550 nm is more than 6 times stronger than the SPR intensity at 850 nm. This significant intensity difference also supports our experimental transmittance results, where the plasmon absorption dip is located within the 500-800 nm wavelength region. Moreover, the EFM results for the nanopillar hybrid film are obtained and shown in Figure S2 at the same wavelengths. The SPR is much weaker in the nanopillar film, where it only occurs on the top portion. By comparing the intensity scale bar for the nanopillar

film with that for the nanomushroom structure, it is noted that the SPR intensity for the nanopillar film is $\sim 10^3$ times weaker than that of the nanomushroom film. This also provides supportive evidence for the disappearance of the absorption curve in the transmittance spectrum of the nanopillar film. The significant degradation of SPR intensity within the nanopillar structure can be attributed to two major reasons: (1) the thickness of the nanopillar structure is much higher than that of the nanomushroom hybrid film, so as the surface plasmon polaritons (SPP) are evanescently confined in the metaldielectric interfaces, they degrade remarkably as they propagate into the crystal lattice and (2) as the interpillar spacing becomes smaller, there will be more wave interference between the nearby SPPs that results in the degradation of SPR effect. 36,37 The SPR data is modeled by COMSOL Multiphysics software, and the schematics and field maps are shown in Figures 5D,E and S3 as the intensities of the SPR effect. The intensity displays that the source of the SPR effect is from the Co mushrooms, particularly the mushroom cap regions. The simulation of VAN pillars shows that the intensity is not significant in the films. SPR comes from the electron oscillation between metallic and dielectric materials. The larger proportion of metallic surface area creates a larger interfacial area with the surrounding dielectric materials that allow for a more intense SPR effect compared to the VAN counterpart. Despite the fact that the absorption peak at 705 nm is relatively small, the peak position is comparable to previous studies on the transmittance data from Co nanocomposite materials with similar peaks reported near 700 nm. $^{38-40}$ This suggests that Co nanomushroom structures in this work present SPR effects.

Although in-plane strain plays an important role in the development of nanocomposites, controlling oxygen present during deposition presents additional control over the growth kinetics of the oxygen phase(s) present. Nanopillar width has been previously controlled through deposition rate, but for nanocomposite systems combining at least one oxide and metal, oxygen partial pressure could be used to control metal nanopillar widths and distribution. As compared to the deposition rate, this method will not work on oxide-oxide systems or metals that are easily oxidized during the deposition process. Using the oxygen partial pressure to control the nanostructure forces the excess metal into formation on the surface of the thin film, e.g., the nanomushroom structure. Nanocomposite thin-film morphology manipulation can finetune materials' properties for future devices and coatings in three dimensions. Adding dimension and texture to thin-film materials can lead to additional functionality that relies on the roughness and nanostructure at the surface of thin films such as self-cleaning and antimicrobial coatings.

CONCLUSIONS

Through growth parameter control (i.e., oxygen partial pressure), a new three-phase metal-oxide—oxideVAN hybrid system of $Co-CeO_2-BTO$ has been demonstrated with tunable film morphology and physical properties. These self-assembled three-dimensional nanostructures, i.e., nanopillars under vacuum growth and nanomushrooms under oxygen partial pressure, open up new possibilities for thin-film materials in exploring functionality tuning. In this case, the magnetization and coercivity of the films tuned from the obvious out-of-plane anisotropy in the vacuum growth sample to very weak paramagnetic nanomushrooms, both under room temperature. In exchange for the weaker magnetic properties,

the nanomushroom structure gained more interesting optical properties in its hyperbolic behavior and SPR effect at the lower end of the visible light spectrum (620–750 nm). The complex three-phase nanocomposite design has great potential in microstructure tuning in hybrid material designs and achieves optimized properties for sensors, dielectrics, memory, and optical waveguides.

ASSOCIATED CONTENT

Supporting Information

The Supporting Information is available free of charge at https://pubs.acs.org/doi/10.1021/acsanm.2c00394.

High-resolution STEM; 3D model of nanomushroom and nanopillar structure films; and cross-sectional and plan-view electric field maps (PDF)

AUTHOR INFORMATION

Corresponding Author

Haiyan Wang — School of Materials Engineering, Purdue University, West Lafayette, Indiana 47907, United States; School of Electrical and Computer Engineering, Purdue University, West Lafayette, Indiana 47907, United States; orcid.org/0000-0002-7397-1209; Email: hwang00@purdue.edu

Authors

Bethany X. Rutherford — School of Materials Engineering, Purdue University, West Lafayette, Indiana 47907, United States; Center for Integrated Nanotechnologies (CINT), Los Alamos National Laboratory, Los Alamos, New Mexico 87545, United States; orcid.org/0000-0003-4149-9891

Bruce Zhang — School of Electrical and Computer Engineering, Purdue University, West Lafayette, Indiana 47907, United States

Matias Kalaswad — School of Electrical and Computer Engineering, Purdue University, West Lafayette, Indiana 47907, United States

Zihao He — School of Electrical and Computer Engineering, Purdue University, West Lafayette, Indiana 47907, United States

Di Zhang — School of Electrical and Computer Engineering, Purdue University, West Lafayette, Indiana 47907, United States; Center for Integrated Nanotechnologies (CINT), Los Alamos National Laboratory, Los Alamos, New Mexico 87545, United States

Xuejing Wang – School of Materials Engineering, Purdue University, West Lafayette, Indiana 47907, United States
Juncheng Liu – School of Materials Engineering, Purdue University, West Lafayette, Indiana 47907, United States

Complete contact information is available at: https://pubs.acs.org/10.1021/acsanm.2c00394

Notes

The authors declare no competing financial interest.

ACKNOWLEDGMENTS

This work was supported by the U.S. Department of Energy, Office of Science, Basic Energy Sciences (BES) under Award DE-SC0020077. The TEM effort is supported by the U.S. National Science Foundation (DMR-2016453 and DMR-1565822). B.X.R. acknowledges the support of Los Alamos National Laboratory and the Office of Science and Graduate

Student Research (SCGSR) Program. Z.H. and H.W. acknowledge the support from the U.S. National Science Foundation (DMR-1809520) for physical property measurements. D.Z. and H.W. acknowledge the support from the Office of Naval Research under Contract No. N00014-20-1-2043 for part of the TEM effort.

REFERENCES

- (1) Misra, S.; Li, L.; Zhang, D.; Jian, J.; Qi, Z.; Fan, M.; Chen, H.; Zhang, X.; Wang, H. Self-Assembled Ordered Three-Phase Au-BaTiO3–ZnO Vertically Aligned Nanocomposites Achieved by a Templating Method. *Adv. Mater.* **2019**, *31*, No. 1806529.
- (2) Paldi, R. L.; Sun, X.; Wang, X.; Zhang, X.; Wang, H. Strain-Driven In-Plane Ordering in Vertically Aligned ZnO Au Nanocomposites with Highly Correlated Metamaterial Properties. ACS Omega 2020, 5, 2234–2241.
- (3) Comes, R.; Liu, H.; Khokhlov, M.; Kasica, R.; Lu, J.; Wolf, S. A. Directed Self-Assembly of Epitaxial CoFe2O4—BiFeO3 Multiferroic Nanocomposites. *Nano Lett.* **2012**, *12*, 2367—2373.
- (4) Fan, M.; Zhang, B.; Wang, H.; Jian, J.; Sun, X.; Huang, J.; Li, L.; Zhang, X.; Wang, H. Self-Organized Epitaxial Vertically Aligned Nanocomposites with Long-Range Ordering Enabled by Substrate Nanotemplating. *Adv. Mater.* **2017**, *29*, No. 1606861.
- (5) Zhang, W.; Ramesh, R.; Macmanus-driscoll, J. L.; Wang, H. Multifunctional, Self-Assembled Oxide Nanocomposite Thin Films and Devices. MRS Bull. 2016, 40, 736–745.
- (6) Sun, X.; Li, Q.; Huang, J.; Fan, M.; Rutherford, B. X.; Paldi, R. L.; Jian, J.; Zhang, X.; Wang, H. Strain-Driven Nanodumbbell Structure and Enhanced Physical Properties in Hybrid Vertically Aligned Nanocomposite Thin Films. *Appl. Mater. Today* **2019**, *16*, 204–212.
- (7) Macmanus-Driscoll, J. L. Self-Assembled Heteroepitaxial Oxide Nanocomposite Thin Film Structures: Designing Interface-Induced Functionality in Electronic Materials. *Adv. Funct. Mater.* **2010**, *20*, 2035–2045.
- (8) Chen, A.; Bi, Z.; Jia, Q.; Macmanus-driscoll, J. L.; Wang, H. Microstructure, Vertical Strain Control and Tunable Functionalities in Self-Assembled, Vertically Aligned Nanocomposite Thin Films. *Acta Mater.* **2013**, *61*, 2783–2792.
- (9) Chen, A.; Su, Q.; Han, H.; Enriquez, E.; Jia, Q. Metal Oxide Nanocomposites: A Perspective from Strain, Defect, and Interface. *Adv. Mater.* **2019**, *31*, No. 1803241.
- (10) Zhang, W.; Chen, A.; Bi, Z.; Jia, Q.; Macmanus-driscoll, J. L.; Wang, H. Interfacial Coupling in Heteroepitaxial Vertically Aligned Nanocomposite Thin Films: From Lateral to Vertical Control. *Curr. Opin. Solid State Mater. Sci.* **2014**, *18*, 6–18.
- (11) Yang, B. H.; Wang, H.; Yoon, J.; Wang, Y.; Jain, M.; Feldmann, D. M.; Dowden, P. C.; Macmanus-driscoll, J. L.; Jia, Q. Vertical Interface Effect on the Physical Properties of Self-Assembled Nanocomposite Epitaxial Films. *Adv. Mater.* **2009**, *21*, 3794–3798.
- (12) Zheng, H.; Straub, F.; Zhan, Q.; Yang, P.; Hsieh, W.; Zavaliche, F.; Chu, Y.; Dahmen, U.; Ramesh, R. Self-Assembled Growth of BiFeO3—CoFe2O4 Nanostructures. *Adv. Mater.* **2006**, *18*, 2747—2752
- (13) Huang, J.; Wang, X.; Hogan, N. L.; Wu, S.; Lu, P.; Fan, Z.; Dai, Y.; Zeng, B.; Starko-bowes, R.; Jian, J.; Wang, H.; Li, L.; Prasankumar, R. P.; Yarotski, D.; Sheldon, M.; Chen, H.; Jacob, Z.; Zhang, X.; Wang, H. Nanoscale Artificial Plasmonic Lattice in Self-Assembled Vertically Aligned Nitride—Metal Hybrid Metamaterials. *Adv. Sci.* 2018, 5, No. 1800416.
- (14) Zheng, H.; Wang, J.; Mohaddes-Ardabili, L.; Wuttig, M.; Salamanca-Riba, L.; Schlom, D. G.; Ramesh, R. Three-Dimensional Heteroepitaxy in Self- Assembled BaTiO3-CoFe2O4 Nanostructures. *Appl. Phys. Lett.* **2004**, *85*, 2035.
- (15) Rutherford, B. X.; Zhang, B.; Wang, X.; Sun, X.; Qi, Z.; Wang, H.; Wang, H. Strain Effects on the Growth of La0.7Sr0.3MnO3 (LSMO)-NiO Nanocomposite Thin Films via Substrate Control. ACS Omega 2020, 5, 23793–23798.

- (16) Zhang, B.; Kalaswad, M.; Rutherford, B. X.; Misra, S.; He, Z.; Wang, H.; Qi, Z.; Wissel, A. E.; Xu, X.; Wang, H. Au-Encapsulated Fe Nanorods in Oxide Matrix with Tunable Magneto-Optic Coupling Properties. ACS Appl. Mater. Interfaces 2020, 12, 51827–51836.
- (17) Wang, X.; Wang, H.; Jian, J.; Rutherford, B. X.; Gao, X.; Xu, X.; Zhang, X.; Wang, H. Metal-Free Oxide-Nitride Heterostructure as a Tunable Hyperbolic Metamaterial Platform. *Nano Lett.* **2020**, *20*, 6614–6622.
- (18) Wang, X.; Jian, J.; Wang, H.; Liu, J.; Pachaury, Y.; Lu, P.; Rutherford, B. X.; Gao, X.; Xu, X.; El-azab, A.; Zhang, X.; Wang, H. Nitride-Oxide-Metal Heterostructure with Self-Assembled Core Shell Nanopillar Arrays: Effect of Ordering on Magneto-Optical Properties. *Small* **2021**, *17*, No. 2007222.
- (19) Su, Q.; Yoon, D.; Sisman, Z.; Khatkhatay, F.; Jia, Q.; Manthiram, A.; Wang, H. Vertically Aligned Nanocomposite La0.8Sr0.2MnO3-x/Zr0.92Y0.08O1.96 Thin Films as Electrode/ Electrolyte Interfacial Layer for Solid Oxide Reversible Fuel Cells. *Int. J. Hydrogen Energy* **2013**, *38*, 16320–16327.
- (20) Yoon, J.; Araujo, R.; Serquis, A.; Caneiro, A.; Zhang, X.; Wang, H.; et al.et al. Nanostructured Cathode Thin Films with Vertically-Aligned Nanopores for Thin Film SOFC and Their Characteristics. Appl. Surf. Sci. 2007, 254, 266–269.
- (21) Yoon, B. J.; Cho, S.; Kim, J.; Lee, J.; Bi, Z.; Serquis, A.; Zhang, X.; Manthiram, A.; Wang, H. Vertically Aligned Nanocomposite Thin Films as a Cathode/Electrolyte Interface Layer for Thin-Film Solid Oxide Fuel Cells. *Adv. Funct. Mater.* **2009**, *19*, 3868–3873.
- (22) Shen, L.; Ma, C.; Cheng, S.; Ren, S.; Cheng, S.; Mi, S.; Liu, M. Enhanced Magnetic Properties in Epitaxial Self-Assembled Vertically Aligned Nanocomposite (Pr0.5Ba0.5MnO3)0.5:(CeO2)0.5 Thin Films. *J. Mater. Chem. C* **2016**, *4*, 10955–10961.
- (23) Huang, J.; Macmanus-driscoll, J. L.; Wang, H. New Epitaxy Paradigm in Epitaxial Self-Assembled Oxide Vertically Aligned Nanocomposite Thin Films. *J. Mater. Res.* **2017**, 32, 4054–4066.
- (24) Shin, J.; Goyal, A.; Cantoni, C.; Sinclair, J. W.; Thompson, J. R. Self-Assembled Ferromagnetic Cobalt/Yttria-Stabilized Zirconia Nanocomposites for Ultrahigh Density Storage Applications. *Nanotechnology* **2012**, *23*, No. 155602.
- (25) Schio, P.; Vidal, F.; Zheng, Y.; Milano, J.; Fonda, E.; Demaille, D.; Vodungbo, B.; Varalda, J.; De Oliveira, A. J. A.; Etgens, V. H. Magnetic Response of Cobalt Nanowires with Diameter below 5 Nm. *Phys. Rev. B* **2010**, 82, No. 094436.
- (26) Vidal, F.; Zheng, Y.; Schio, P.; Bonilla, F. J.; Barturen, M.; Milano, J.; Demaille, D.; Fonda, E.; De Oliveira, A. J. A.; Etgens, V. H. Mechanism of Localization of the Magnetization Reversal in 3 Nm Wide Co Nanowires. *Phys. Rev. Lett.* **2012**, *109*, No. 117205.
- (27) Bonilla, F. J.; Novikova, A.; Vidal, F.; Zheng, Y.; Fonda, E.; Demaille, D.; Schuler, V.; Coati, A.; Vlad, A.; Garreau, Y.; Simkin, M. S.; Dumont, Y.; Hidki, S.; Etgens, V. Combinatorial Growth and Anisotropy Control of Self-Assembled Epitaxial Ultrathin Alloy Nanowires. *ACS Nano* 2013, 7, 4022–4029.
- (28) Huang, J.; Li, L.; Lu, P.; Qi, Z.; Sun, X. Self-Assembled Co-BaZrO3 Nanocomposite Thin Films with Ultra-Fine Vertically Aligned Co Nanopillars. *Nanoscale* **2017**, 7970–7976.
- (29) Park, J. H.; Jang, H. M.; Kim, H. S.; Park, C. G.; Lee, S. G. Strain-Mediated Magnetoelectric Coupling in BaTiO3-Co Nanocomposite Thin Films. *Appl. Phys. Lett.* **2008**, *92*, No. 062908.
- (30) Myagkov, V. G.; Zhigalov, V. S.; Bykova, L. E.; Zharkov, S. M.; Matsynin, A. A.; Volochaev, M.; Volochav, M. N.; Tambasov, I. A. Thermite Synthesis and Characterization of Co-ZrO2 Ferromagnetic Nanocomposite Thin Films. *J. Alloys Compd.* **2016**, *665*, 197–203.
- (31) Zeng, S.; Baillargeat, D.; Ho, H.; Yong, K. Nanomaterials Enhanced Surface Plasmon Resonance for Biological and Chemical Sensing Applications. *Chem. Soc. Rev.* **2014**, *43*, 3426–3452.
- (32) Rhodes, C.; Franzen, S.; Maria, J.-P.; Losego, M.; Leonard, D. N.; Laughlin, B.; Duscher, G.; Weibel, S. Surface Plasmon Resonance in Conducting Metal Oxides. *J. Appl. Phys.* **2006**, *100*, No. 054905.
- (33) Silva, D. O.; Scholten, J. D.; Gelesky, M. A.; Teixeira, S. R.; Dos Santos, A. C. B.; Souza-Aguiar, E. F.; Dupont, J. Catalytic Gas-to-

- Liquid Processing Using Cobalt Nanoparticles Dispersed in Imidazolium Ionic Liquids. ChemSusChem 2008, 1, 291–294.
- (34) Wolf, M.; Kotz, H.; Fischer, N.; Claeys, M. Size Dependent Stability of Cobalt Nanoparticles on Silica under High Conversion Fischer—Tropsch Environment. *Faraday Discuss.* **2017**, *197*, 243—268. (35) Gray, N. W.; Tiwari, A. Dynamic Superparamagnetism in Cobalt Doped Sm2O3 Thin Films. *J. Appl. Phys.* **2013**, *110*, No. 033903.
- (36) Zhu, P.; Shi, H.; Guo, L. J. SPPs Coupling Induced Interference in Metal/Dielectric Multilayer Waveguides and Its Application for Plasmonic Lithography. *Opt. Express* **2012**, *20*, 12521–12529.
- (37) Zhang, D.; Lu, P.; Misra, S.; Wissel, A.; He, Z.; Qi, Z.; Gao, X.; Sun, X.; Liu, J.; Lu, J.; Zhang, X.; Wang, H. Design of 3D Oxide—Metal Hybrid Metamaterial for Tailorable Light—Matter Interactions in Visible and Near-Infrared Region. *Adv. Opt. Mater.* **2021**, *9*, No. 2001154.
- (38) Maruyama, T.; Arai, S. Electrochromic Properties of Cobalt Oxide Thin Films Prepared by Chemical Vapor Deposition. *J. Electrochem. Soc.* **1996**, *143*, No. 1383.
- (39) Du, G. X.; Mori, T.; Suzuki, M.; Saito, S.; Fukuda, H.; Takahashi, M. Magneto-Optical Effects in Nanosandwich Array with Plasmonic Structure of Au/[Co/Pt]n/Au. *J. Appl. Phys.* **2010**, *107*, No. 09A928.
- (40) Gonzalez-Nelson, A.; Joglekar, C.; Van Der Veen, M. A. Pillared Cobalt Metal-Organic Frameworks Act as Chromatic Polarizers. *Chem. Commun.* **2021**, *57*, 1022–1025.

□ Recommended by ACS

Controlled Porosity in Ferroelectric BaTiO3 Photoanodes

Adriana Augurio, Joe Briscoe, et al.

MARCH 10, 2022

ACS APPLIED MATERIALS & INTERFACES

READ 🗹

Effect of BaCO3 Impurities on the Structure of BaTiO3 Nanocrystals: Implications for Multilayer Ceramic Capacitors

Tedi-Marie Usher, Katharine Page, et al.

SEPTEMBER 02, 2020

ACS APPLIED NANO MATERIALS

READ 🗹

Control of Layering in Aurivillius Phase Nanocomposite Thin Films and Influence on Ferromagnetism and Optical Absorption

Lutz Mühlenbein, Akash Bhatnagar, et al.

APRIL 12, 2022

ACS APPLIED ELECTRONIC MATERIALS

READ **C**

Rational Co-Doping of SrZrO3 and BaTiO3 in Bi0.5Na0.5TiO3 for Extraordinary Energy Storage and Electrocaloric Performances

Ying Hou, Junfeng Ding, et al.

FEBRUARY 20, 2022

ACS APPLIED ENERGY MATERIALS

READ 🗹

Get More Suggestions >